ELSEVIER

Journal of Nuclear Materials 220–222 (1995) 244–248

journal of nuclear materials

Comprehensive model for disruption erosion in a reactor environment ☆

A. Hassanein [a], I. Konkashbaev [b]

[a] *Argonne National Laboratory Argonne, IL 60439, USA*
[b] *Troitsk Institute for Innovation, Russian Federation*

Abstract

A comprehensive disruption erosion model which takes into account the interplay of major physical processes during plasma–material interaction has been developed. The model integrates with sufficient detail and in a self-consistent way, material thermal evolution response, plasma–vapor interaction physics, vapor hydrodynamics and radiation transport in order to realistically simulate the effects of a plasma disruption on plasma-facing components. Candidate materials such as beryllium and carbon have been analyzed. The dependence of the net erosion rate on disruption physics and various parameters was analyzed and is discussed.

1. Introduction

The behavior of plasma-facing materials (PFMs) during a major disruption is critical for successful and reliable operation of a reactor. During the rapid thermal quench (≈ 100 μs) of a disruption, energetic plasma electrons and ions strike parts of the divertor plate, depositing energy densities of 10–100 MJ/m^2 and thus causing surface melting and ablation. If all of the incident energy were to be deposited entirely in the PFM, extensive ablation would severely limit the lifetime of the divertor plate and critically diminish the economic feasibility of the reactor.

However, it is expected that the initial wave of the ablated material will form a vapor cloud in front of the incoming plasma particles, thereby reducing the energy flux to PFMs and consequently prolong its lifetime substantially. Several analyses of this vapor shielding effect have been performed [1–7]. Some previous work focused on one or two separate areas of the various processes involved during plasma–material interaction. Other work has focused separately on issues such as radiation transport [8], simulation experiments [9], and magnetic field effects [10].

Three major areas must be investigated to correctly evaluate material response during a plasma disruption. These are: target material thermodynamic response, vapor cloud hydrodynamics, and radiation transport. Fig. 1 is a schematic illustration of the various interaction zones and processes that occur during the plasma/material interaction following a disruption. Basically this problem involves three moving boundaries: the vapor front, the receding surface, and the solid–liquid interface. These three moving boundaries are interdependent and a complete solution should link them dynamically and simultaneously. Models for thermal evolution of a material, plasma/vapor interaction physics, vapor hydrodynamics, and radiation transport have been developed, integrated, and perfected in a self-consistent way in sufficient detail to realistically simulate the effect of a disruption on plasma-facing components. Candidate PFMs such as beryllium and carbon were considered in this analysis. The effect of uncertainties in reactor disruption conditions on the net erosion rate was also analyzed.

☆ Work supported by the United States Department of Energy, Office of Fusion Energy, under Contract W-31-109-Eng-38.

SSDI 0022-3115(94)00421-8

2. Physical model

2.1. Material thermal evolution

The thermal response of the PFM is calculated by solving a time-dependent heat conduction equation in one-or two-dimensional coordinates [11]. For simplicity, the heat conduction equation in the one-dimensional form (y being the direction perpendicular to the surface) can be given by

$$\rho c_p \frac{\partial T}{\partial t} = \nabla \cdot (K \nabla T) + \dot{q}(y, t), \tag{1}$$

where ρ is the density, c_p is the specific heat, K is the thermal conductivity, and q is the volumetric energy deposition rate of the energetic plasma ions and electrons. All thermophysical properties are assumed to be a function of local temperature. Surface temperature was determined by both the boundary conditions and the evaporation process. The boundary condition at the surface can then be given by

$$-K \frac{\partial T}{\partial y}(o, t) = q_{gas} + q_{rad} - q_{evap}, \tag{2}$$

where q_{gas} is the net heat flux from the near-wall vapor zone; q_{rad} is the radiation heat flux absorbed at the material surface; and q_{evap} is the evaporated heat flux, as determined by the enthalpy of evaporation. The evaporation flux leaving the surface is calculated in detail from models developed under nonequilibrium conditions [2,18].

The volumetric energy deposition function $q(y, t)$ is calculated, in the condensed target material, with detailed models that include the slowing-down physics of plasma particles (both ions and electrons) in various target materials [5]. Phase change of metallic materials, when temperature exceeds their melting points are calculated using previously developed models [12,13].

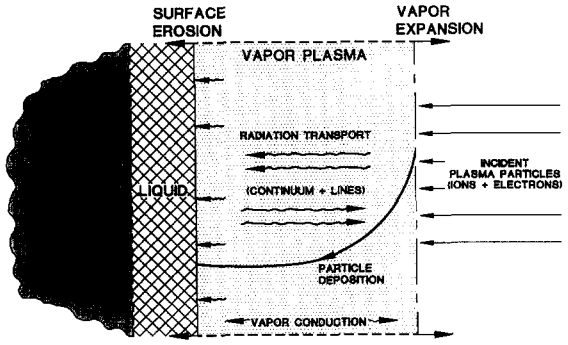

Fig. 1. Schematic illustration of various interaction zones and processes during a plasma disruption.

The net heat flux q_{gas}, due to particle transport from the near-surface vapor to the target, is described by a free-streaming energy transport term according to [14,15]

$$q_{gas} = \alpha \tfrac{1}{4} n_i v_i \tfrac{3}{2} k (T_i - T_s), \tag{3}$$

where v_i is ion thermal velocity, T_i is ion temperature, T_s is the target surface temperature, and α is a collisional modification factor (accommodation coefficient $\alpha \approx 0.2$) of the free-streaming energy transport.

2.2. Vapor plasma hydrodynamics

The extent of vapor expansion into the vacuum vessel is determined by solving the vapor hydrodynamic equations for conservation of mass, momentum, and energy:

$$\frac{\partial \rho}{\partial t} + \nabla \cdot (\rho V) = 0, \tag{4}$$

$$\rho \frac{\partial V}{\partial t} + \nabla P = 0, \tag{5}$$

and

$$\frac{\partial E}{\partial t} + \nabla \cdot (EV) + P \nabla \cdot V = \nabla \cdot (K \nabla T) + \nabla \cdot Q_r + \nabla \cdot Q_b, \tag{6}$$

where V is the vapor velocity, K is the vapor conductivity, Q_r is the radiation flux, and Q_b is the plasma particle beam flux. All variables of these equations are both time and space dependent. The solution of these equations is approximated by finite difference methods described in Ref. [15]. The plasma beam particle flux deposited in the vapor is calculated by similar methods for slowing down in a cold target, i.e., by inelastic and elastic collisions; however an additional stopping mechanism is used which arises from the free electrons due to ionization. This free electron stopping term can substantially shorten the range of both plasma ions and electrons in the ionized vapor leading to high energy deposition rate at the front of the vapor zone.

2.3. Radiation transport

It is the radiation transport that will finally determine the net energy flux to PFMs and, consequently, determine the net erosion rate and lifetime of the divertor plate. It is then important to correctly model the radiation transport for a wide range of vapor conditions. For quasistationary conditions, the transport equation for the radiation has the form

$$\Omega \nabla I_v = \epsilon_v - \kappa_v I_v, \tag{7}$$

where I_v is radiation intensity, v is frequency, ϵ_v is vapor emissivity, Ω is the solid angle, and κ_v is the

absorption coefficient. Several methods are available for solving radiation transport equations. However, the most convenient one is the so-called forward-reverse method [16]. The main advantage of this method is a better description of both the optically thin and the optically thick plasma conditions [17]. Other popular methods, such as diffusion approximation are valid only for optically thick plasma conditions. The forward–reverse method treats the photon flux moving to the right (forward) I_ν^+ separately from the photon flux moving to the left (reverse) I_ν^-. Assuming one-dimensional plane geometry, and after integrating over the angles, the radiation fluxes in the forward and reverse direction are calculated for each vapor zone as

$$\frac{1}{2}\frac{\mathrm{d}I_\nu^\pm}{\mathrm{d}y} = \epsilon_\nu - \kappa_\nu I_\nu^\pm. \tag{8}$$

In these calculations, the radiation fluxes are composed of two separate components, continuum radiation flux I_{c_ν} and lines radiation flux I_{l_ν}, so that

$$I_\nu^\pm = I_{c\nu}^\pm + I_{l\nu}^\pm. \tag{9}$$

Therefore, the most intense lines are treated separately using the collisional radiative equilibrium (CRE) method. This is because the vapor cloud plasma is not in local thermodynamic equilibrium (LTE). The atomic level populations are not obtained from the Saha equation and Boltzmann distributions. A set of rate equations is therefore solved for the populations of each individual atomic level. The less intense lines are combined with the continuum radiation. Multigroup approximations (1000–4000 photon groups) were used for the continuum solution of the above equations. Opacity and emissivity data are provided in the form of tables for a wide range of expected vapor densities and temperatures. The rate of energy loss due to radiation Q_r in each zone can then be given by

$$Q_r = \frac{1}{\rho}\sum_\nu \nabla\cdot(I_\nu^+ + I_\nu^-). \tag{10}$$

3. Results

The comprehensive self-consistent model described above is implemented in a new optimized version of the computer code A*THERMAL-S. In this analysis the thermal quench time during a disruption is assumed to be 100 μs. Plasma energy densities of 10–100 MJ/m^2 are used in this analysis. Fig. 2 shows the time evolution of beryllium surface temperature, melt layer thickness, and eroded thickness for a disruption with 20 keV plasma electrons and 10 MJ/m^2 energy density. The sudden early rise in surface temperature is due to direct electron energy deposition in beryllium.

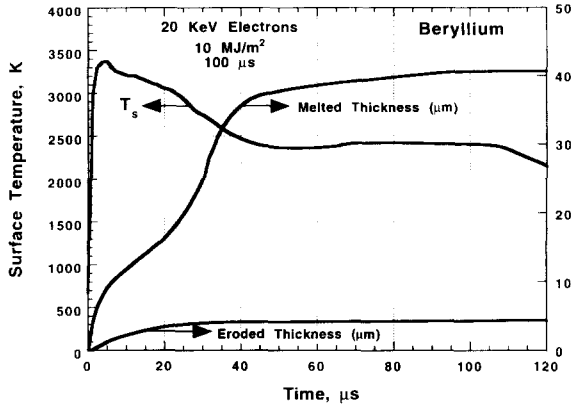

Fig. 2. Change in beryllium surface temperature, melt layer, and eroded thickness with time, following exposure to plasma electrons.

The following decrease in the beryllium surface temperature was caused by the shielding effect of the eroded material above the beryllium surface. The flat temperature behavior during the rest of the disruption was mainly due to the low generated radiation heat flux in this case. The net ablation erosion rate for the given disruption conditions is about 4 mm, which is substantially lower than that without the shielding effect [13].

Fig. 3 shows the relationship of beryllium solid–liquid–vapor temperatures to distance at two times, i.e., 10 μs and 100 μs, during the disruption. At an early time (10 μs) the solid temperature was higher than at later times because of the direct deposition of plasma electrons. The temperature of the vapor layer at that time was relatively low (≈ 1 eV) and the vapor layer only expanded to about 3–4 cm above the surface. At longer times, towards the end of the disruption, the solid–liquid temperature was lower because

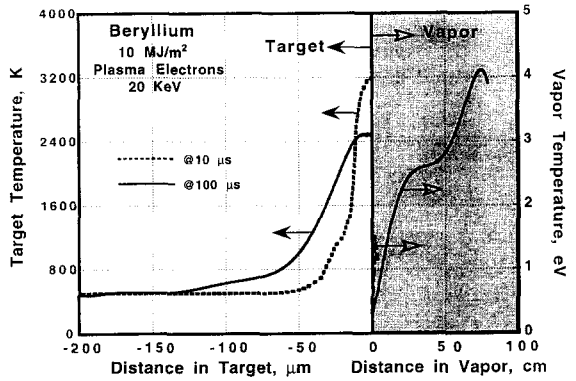

Fig. 3. Relationship of target and vapor temperature to distance at different times during disruption.

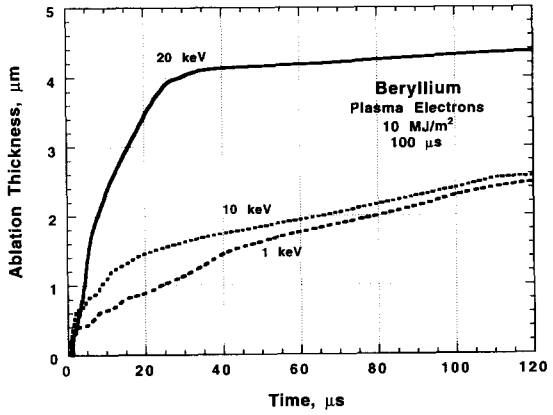

Fig. 4. Effect of plasma electron kinetic energy on beryllium erosion rate.

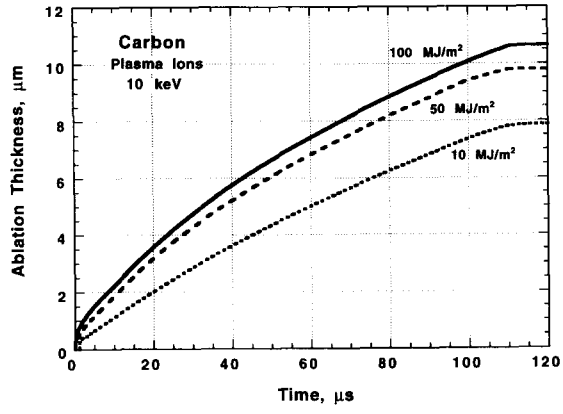

Fig. 5. Effect of higher disruption energy densities on carbon erosion rate.

only a small fraction of the radiation energy was deposited on the surface. The vapor had then expanded to distances up to 70 cm above the surface and reached a temperature of ≈ 4 eV.

Fig. 4 shows the effect of plasma-electron kinetic energy on the erosion rate. Particles with higher kinetic energy usually penetrate the target to a greater depth and result in more erosion rate. However, because more material is eroded by high-energy particles, the vapor will have a lower temperature and, consequently, emit less radiation flux toward the PFM. This is evident from the slope of ablated thickness in Fig. 4. Particles with lower kinetic energy erode less material and, for the same energy density, result in higher vapor temperatures and thus higher radiation fluxes [19]. The difference between the effect of plasma electrons and plasma ions, with similar kinetic energy on the beryllium erosion rate was also studied. Basically, ions with higher kinetic energy (20 keV) behave in a manner similar to that of electrons with lower kinetic energy (1 keV), where the front vapor zone is heated to higher vapor temperatures and results in some radiation flux reaching the PFM surface. This is due to the fact that ions have much shorter range than electrons with the same kinetic energy. Ions then produce less erosion than electrons with similar initial kinetic energy.

The energy density reaching the divertor plate during a disruption can be much higher than 10 MJ/m^2 [21]. Fig. 5 shows the effect of higher energy densities (up to 100 MJ/m^2) on the erosion rate of carbon. An order-of-magnitude increase in energy density resulted in an increase of only $\approx 30\%$ in erosion rate. This is mainly because most of the incident energy was used to heat the front regions of the vapor [19]. It was also found that, for the same heat flux, carbon erodes more than beryllium; this is because carbon radiates energy more than beryllium which results in more net radiation flux to the PFM and higher free-streaming energy flux from the near-wall vapor zone. However, beryllium melts, and erosion of the melt layer during the disruption can be of serious concern [20]. Fig. 6 shows carbon and beryllium erosion rates at various disruption energy densities. If the melt layer is lost during the disruption, beryllium erosion is about 5 times higher than that of carbon for the disruption conditions of this study. If the melt layer is lost as soon as it develops, however, disruption lifetime can be significantly reduced.

Further analysis and investigation are needed for a number of important issues related to modeling erosion depth during a disruption. One important issue is the effect of an oblique magnetic field on the hydrodynamics of the vapor cloud that develops during a disruption. A 2-D magnetohydrodynamic model was recently developed and integrated with this model to study such an effect on the net erosion rate; prelimi-

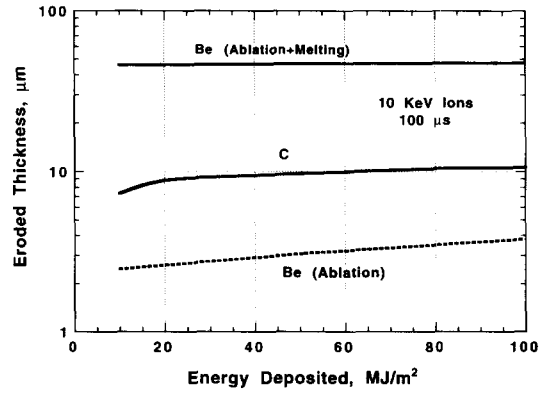

Fig. 6. Erosion rate of beryllium and carbon at various disruption energy densities.

nary analysis indicates that the magnetic field may reduce the overall erosion rate [21]. Another important factor that can affect erosion depth is the two-dimensional effects of radiation transport in the vapor cloud. A 2-D radiation transport model was recently developed and integrated with this model [22]. It is found that escaping lateral radiation from the vapor cloud can significantly reduce the net heat flux to the PFM, thus reducing the erosion rate.

4. Conclusion

A comprehensive self-consistent model was developed to take into account the various interaction zones/processes that occur during a disruption. Models for material thermal evolution with phase change, vapor hydrodynamics, and radiation transport, including line radiations, are dynamically integrated, perfected, and numerically optimized for realistic and efficient simulation of disruption effects.

Results of disruption simulation indicate that plasma electrons, can cause higher erosion rates than plasma ions having the same initial kinetic energy. Carbon ablation thickness is usually higher than that of beryllium under similar conditions. However, if the beryllium melt layer is lost during the disruption, beryllium erosion will be much higher than that of carbon-based materials. Higher disruption energy densities will generally result in a modest increase in erosion rate compared to an increase in energy density.

Acknowledgements

The authors sincerely thank Dr. G. Romanov, Dr. B. Bazilev, and Dr. V. Tolkach of the Institute of Heat and Mass Transfer at the Belorussia Academy of Science, Minsk, for their help in supplying the data on opacity and emissivity for this analysis.

References

[1] A. Sestero and A. Ventura, J. Nucl. Mater. 128/129 (1984) 828.
[2] A. Hassanein et al., Nucl. Eng. Design/Fusion 1 (1984) 307.
[3] B.J. Merrill and J.L. Jones, J. Nucl. Mater. 111/112 (1982) 544.
[4] H. Bolt et al., J. Nucl. Mater. 196–198 (1992) 948.
[5] A. Hassanein and D. Ehst, J. Nucl. Mater. 196–198 (1992) 680.
[6] B. Goel et al., Fusion Technol. (1992) 272.
[7] W. Höbel et al., J. Nucl. Mater. 196–198 (1992) 537.
[8] R.R. Peterson, UWFDM-357 (1983).
[9] A. Hassanein et al. J. Nucl. Mater. 212–215 (1994) 1272.
[10] J. Gilligan and D. Hahn, J. Nucl. Mater. 145–147 (1987) 391.
[11] A. Hassanein, J. Nucl. Mater. 122/123 (1984) 1453.
[12] A. Hassanein and D. Smith, J. Nucl. Mater. 191–194 (1992) 503.
[13] A. Hassanein, ASME, 88-WA/NE-2.
[14] R.J. Procassini and C.K. Birdsall, Phys. Fluids B 3 (1991) 1876.
[15] Y.L. Igitkhanov et al., Sov. J. Plasma Phys. 12 (1) (1986).
[16] B.N. Chetverushkin, Mathematical modelling of the radiative gas (Nauka, Moscow, 1986).
[17] I.V. Nemchinov, VINITI, N1721-83, Moscow, 1983.
[18] S.I. Anisimov and A.Kh. Rakhmatulina, Sov. Phys. JETP, vol. 37 (1973) 441.
[19] A. Hassanein and I. Konkashbaev, Argonne National Laboratory Report, ANL/FPP/TM-271, October 1994.
[20] A. Hassanein, Fusion Technol. 15 (1989) 513.
[21] A. Hassanein and I. Konkashbaev, 3rd Int. Symp. on Fusion Nuclear Technology (ISFNT-3), Los Angeles, California, 1994, to be published in Fusion Eng./Design.
[22] A. Hassanein, 11th Topical Meeting on the Technology of Fusion Energy, ANS, 1994, to be published in Fusion Technol.